New results on the core-halo spatial structure in ^{6}He and ^{8}He from proton elastic scattering

F. Aksouh[1]*, O.A. Kisselev[1,2], A. Bleile[1], O.V. Bochkarev[3], L.V. Chulkov[3], D. Cortina-Gil[1]†, A.V. Dobrovolsky[1,2], P. Egelhof[1], H. Geissel[1], M. Hellström[1], N.B. Isaev[2], B.G. Komkov[2], M. Màtos[1], F.V. Moroz[2], G. Münzenberg[1], M. Mutterer[4], V.A. Mylnikov[2], S.R. Neumaier[1], V.N. Pribora[3], D.M. Seliverstov[2], L.O. Sergueev[2], A. Shrivastava[1]‡, K. Sümmerer[1], H. Weick[1], M. Winkler[1] and V.I. Yatsoura[2]

[1] *Gesellschaft für Schwerionenforschung mbH, D-64291 Darmstadt, Germany*

[2] *Petersburg Nuclear Physics Institute, RU-188350 St. Petersburg, Russia*

[3] *Russian Research Center "Kurchatov Institute", RU-123182 Moscow, Russia*

[4] *Institut für Kernphysik, Technische Universität, D-64289 Darmstadt, Germany*

10th International Conference on Nuclear Reaction Mechanisms, Varenna, Villa Monastero, June 9-13, 2003

Abstract

The differential elastic proton scattering cross section was measured up to the region of the first diffraction minimum in an inverse kinematic experiment by using relativistic radioactive beams of $^{6,8}He$ incident on a liquid-hydrogen target. Nuclear matter density distributions were obtained with good accuracy by using the Glauber diffractive multiple scattering theory. They allow, in particular, to have a new detailed insight into the spatial core-halo structure in these nuclei.

1 Introduction

Since the middle of the 80's, secondary beams of radioactive nuclei have been used to study short-lived nuclei, in particular, those close to the neutron dripline like $^{6,8}He$ which show features of halo structure [1, 2]. The first measurement was to determine the interaction cross sections, then the fragmentation cross sections, momentum distribution of fragments and proton elastic scattering. The latter [3, 4, 5] turned out to be an efficient tool when applied at intermediate energies, around 0.7 GeV/u, to scan the radial distribution of nuclear matter at the periphery of the nucleus. Therefore such measurements demonstrated the halo structure of $^{6,8}He$. The accurate study of the central part of these nuclei remained challenging mainly when theoretical investigations [6] predicted a high sensitivity on the parameters of the nuclear matter densities for the $p(^{6,8}He)$ differential cross sections at scattering angles in the region of the first diffraction minimum of the angular distribution.

To illustrate this fact, a simulation calculation of the $p(^{8}He)$ elastic differential cross section at 671 MeV/u is shown in Fig. 1. Two different approaches were used leading to two extreme pictures of ^{8}He. In the COSMA model [7], a strongly bound α-core inside the nucleus is surrounded by four valence halo neutrons leading to a large difference in the proton- and neutron distributions. In the DISS picture, the proton and neutron distributions have similar radii for the same total size, therefore the core and halo components are completely dissolved. While for the low momentum transfer $(0.002 < -t < 0.05 (GeV/c)^2)$, it is difficult to distinguish between the two different approaches for the intrinsic structure of ^{8}He, the situation is different for the higher t region. The position of the first minimum and the slope of the cross section are very sensitive to the

*__Corresponding author__, E-mail address: farouk.aksouh@fys.kuleuven.ac.be __Present address__: Instituut voor Kern- en Stralingsfysika, K. U. Leuven, Celestijnenlaan 200D, B-3001 Leuven, Belgium

†__Present address__: Depto. de Fisica de Particulas, Universidade de Santiago de Compostela, E-15706 Santiago de Compostela, Spain

‡__Present address__: Nuclear Physics Division, Bhabha Atomic Research Centre, Trombay, IN-400085 Mumbai, India

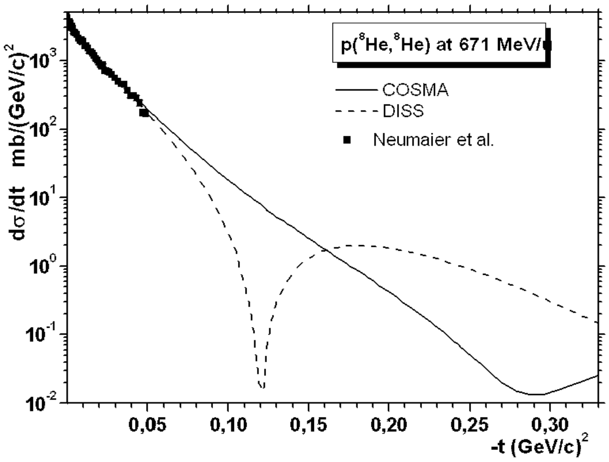

Figure 1: *Calculated differential elastic cross section for the p(^8He) scattering at 671 MeV/u. Experimental data (full squares) are taken from Ref. [4]. The ^8He nucleus is depicted as an α+4n system (COSMA) with spatially well defined core and halo nucleons and as a system where the core is dissolved (DISS)*

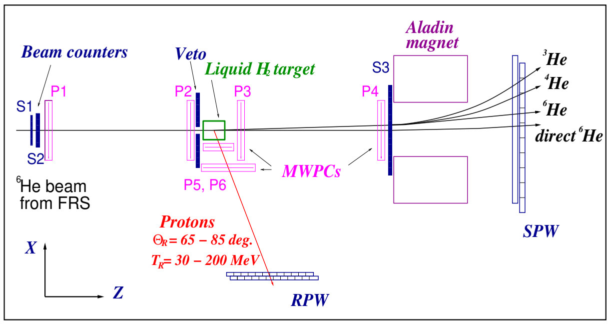

Figure 2: *Schematic representation of the experimental setup.*

shape of the density distribution and, within the model, strongly correlated with the size of the core.

2 Experimental setup and determination of the cross sections

The secondary beams were produced from the fragmentation of a primary ^{18}O beam with respective energies 820 and 730 MeV/u at a rate of 2×10^{10} pps on a ^9Be production target of 8 g/cm^2 thickness. $^{6,8}He$ beams were selected through the FRagment Separator (FRS) [8] at energies around 717 MeV/u and 671 MeV/u respectively. For these high magnetic rigidities (13.9 and 17.5 Tm), the FRS is the only available facility worldwide offering such possibilities. The beams were then directed to the experimental area in Cave B with average intensities $1.9 \cdot 10^5$ and $1.6 \cdot 10^4$ pps, respectively. The calculated ^6He beam divergency at the entrance of the experimental setup is larger compared to stable beams, 3.4 and 6.8 mrad in the X and Y directions, respectively, which required to have a precise tracking. The experimental setup is displayed in Fig. 2

The passage of a beam particle is determined by two small-sized scintillators S1, S2 before the target and a bigger one, S3 after. It is also vetoed right before interacting, by means of a big scintillator plate with a 2 cm diameter hole. The passage of the recoil protons is determined with the anode signals from the multiwire proportional chambers (MWPCs) P5 and P6. These two events form a two-step trigger required to record the data.

The angular resolution for the scattering angle is a strong requirement since the scattering is concentrated in the forward direction (typically in a cone of 4°) while the recoil protons are emitted laterally with energies ranging from 30 MeV up to 200 MeV. A precise (150 μm resolution) position measurement is done via three pairs of MWPCs, (P1,P2), (P3,P4) and (P5,P6) in order to track the incident and scattered beam particle and the recoil proton respectively. A large position sensitive scintillator wall (RPW) was positioned 2.3 m from the target. It has two layers of vertical slats (length×width×thickness = 110 cm × 2.5 cm × 1 cm) shifted by a half-width to each other, thus allowing an angular resolution of 5.43 mrad (0.3°).

The needed angular resolution requires to have large gaps between MWPCs P1 and P2, P3 and P4 and between P6 and the RPW, typically 2 m separation. This causes angular straggling due to air so all the corresponding space was filled with He gas at atmospheric pressure.

Principally, different nuclear levels may be excited and this can lead to a complicated analysis. Fortunately, all excited states in $^{6,8}He$ are particle unstable, therefore it is sufficient to select the elastically scattered particles from the resulting fragments or from the products of break-up and knock-out reactions by performing a magnetic separation after the interaction (Dipole magnet ALADIN). Another position sensitive scintillator wall (SPW) was positioned perpendicular to the beam direction at 2.3 m upstream from the dipole exit window.

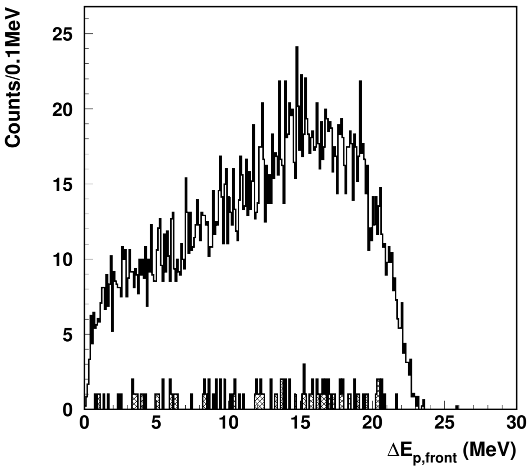

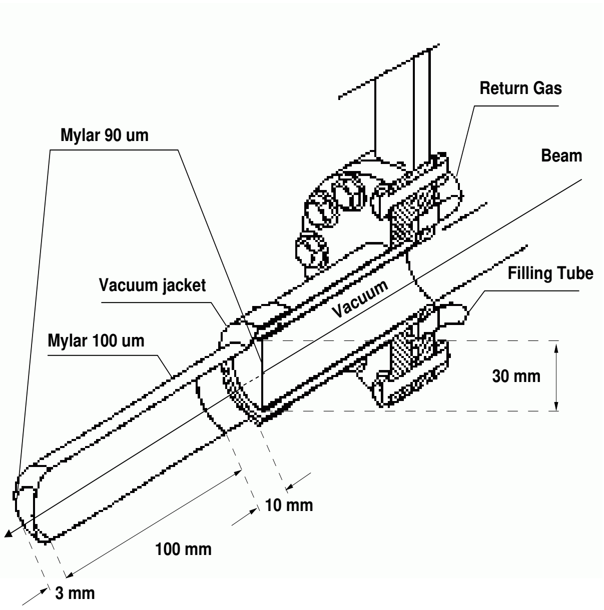

Figure 3: On top, spectra of the elastic proton energy loss $\Delta E_{p,front}$ in the RPW front layer with filled and empty (hatched) target from the interaction of ^6He. The spectra are normalized to the same flux of incident particles. The bottom figure shows a longitudinal cut of the target cell.

The liquid-hydrogen (LH_2) target cell (Fig. 3 bottom) and the necessary cryogenic and command ensembles were designed and built at the cryogenics division of CEA (France). The system is modular and can therefore work with different cell geometries. The cell is mounted in a vacuum chamber with thin windows to limit angular and energy straggling and offers the largest possible solid angle. The effective thickness of the target was about 708 mg/cm^2. The target can be operated in an "empty mode" for background measurements. The key-feature is a low background level (Fig. 3 top) as compared to classical $(CH_2)_n$ targets. The few events seen in the empty mode are related to the presence of a small quantity of H_2 gas[1].

The top part of Fig. 4 shows how the separation of the elastic events is performed. Using the energy loss in the SPW, particles with nuclear charge Z=2 are selected and the tracking data from the MWPCs together with the position measured on the SPW are further used to select the candidate events. Finally, one checks that these events agree kinematically with a two-body elastic scattering picture (bottom part of Fig. 4).

Two major corrections have to be applied: (i) since the setup has no cylindrical symmetry, one has to correct for different solid angles at different scattering angles and (ii) due to loss of MWPCs efficiency for high energy recoil protons where the energy loss was in the order of the anode threshold, one must correct by adding the contribution which was lost. The latter contribution was determined by using a Monte-Carlo simulation in which the exact experimental conditions were used. The correction is negligible at $-t \simeq 0.05(GeV/c)^2$ with an efficiency factor of about 1.00 ± 0.03 while it is important at $-t \simeq 0.19(GeV/c)^2$ with a factor around 0.08 ± 0.04 meaning 50% of additional relative uncertainty on those data.

The differential cross section $\frac{d\sigma}{dt}$ defined versus the momentum transfer $t = -q^2$ is given by:

$$\frac{d\sigma}{dt} = \frac{1}{N_B \cdot N_T} \cdot \frac{dN}{dt} \qquad (1)$$

where N_B is the total number of incident beam particles, N_T is the number of proton nuclei in the target per unit area and dN is the total number of elastic events detected in the interval dt. The target density was determined to be $\rho = 0.0700(13)\ g/cm^3$. The formulation in Eq. 1 is valid for a thin target approximation for which the interaction probability $P_{int} = A{\cdot}\sigma_{int}{\cdot}\Delta z \ll 1$. Here $A = \rho \cdot \aleph_{AV}/M_H$ is a constant characteristic of the target material, $\aleph_{AV}$ is the Avogadro number, M_H the hydrogen molar mass, Δz the target thickness and σ_{int} is the total interaction cross section of $^{6,8}He$ on a hydrogen target. Taking σ_{int} to be 198.9 mb and 252.0 mb

[1]At the target temperature 20 K, the H_2 gas to liquid density ratio is 1/55

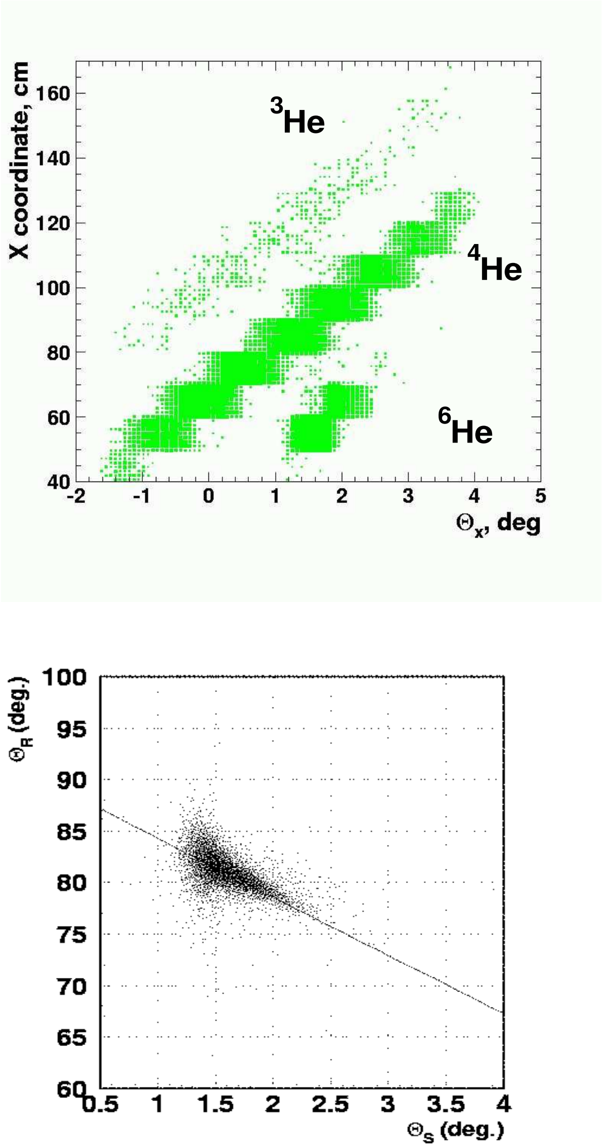

Figure 4: On top, correlation plot showing the X coordinate from the SPW versus the X component Θ_x of the scattering angle for the ^6He run. The bottom figure shows the two-body kinematic correlation (solid line) between the recoil and scattering angles once the ^6He elastic events are selected from the top plot.

[4] for ^6He and ^8He respectively, the interaction probability is 0.09 (9%) for a thickness Δz=10.8 cm which means that the target must be considered as thick. The Eq. 1 underestimates the cross section, therefore the cross section must be corrected by a factor 1.05(2).

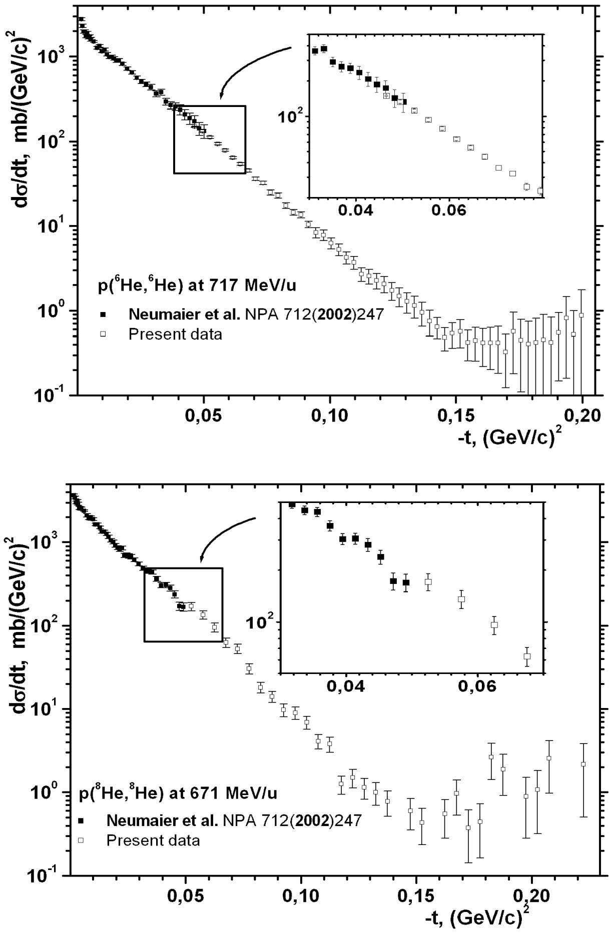

Figure 5: Experimental p(^6He,^6He) differential cross section at 717 MeV/u (top) and p(^8He,^8He) differential cross section at 671 MeV/u (bottom) versus the four-momentum transfer $-t$. The present data (open square) coincide nicely with the data at low momentum transfer (black squares taken from Ref. [4]). The insert shows the region of overlap in more detail.

The experimental cross sections determined from this preliminary analysis are shown in Fig. 5. The errors represent contributions from statistical uncertainties and errors from efficiency correction of the MWPCs. These errors are t dependent and in particular higher in the region of the first minimum. Sources of systematical errors, independent of t, arise from the absolute normalization of the data, namely from the determination of the target thickness and density. The relative systematical uncertainty amounting to 2.4% are included in the fit analysis (see the Ref. [14] for details) in the form of an additional independent parameter.

3 Nuclear matter densities and radii

At intermediate energy and with a simple hadronic probe such as a proton, the scattering mechanism is rather simple and can be treated with a multiple-scattering description such as the one developed by Glauber and Sitenko (see principles and details in the review article [9], or in chapter 6 of [10] and references therein, or in [11, 12]). The physical conditions which hold at intermediate energy permit the use of the adiabatic approximation where one assumes the internal nucleons fixed during the interaction since the projectile energy is high enough compared to their mean kinetic energy. In-medium effects are assumed to be negligible which means that during the interaction inside the nucleus, the proton encounters, in average, multiple scattering on free nucleons. It is therefore possible to relate the differential elastic cross section $\frac{d\sigma}{dt}$ to the nuclear matter density distribution in an unequivocal way.

The calculation of the differential cross sections requires the knowledge of the free elementary proton-proton (pp) and proton-neutron (pn) interaction parameters. Only the scalar part of the corresponding scattering amplitudes are used. These are parametrized [5] by complex gaussians:

$$f_{pN}(\mathbf{q}) = \frac{ik}{4\pi}\sigma_{pN}(1 - i\varepsilon_{pN})e^{-q^2\beta_{pN}/2} \qquad (2)$$

with $\mathbf{q}$ being the momentum transfer, σ_{pN} the total free proton-nucleon (pN) elastic cross section, $\varepsilon_{pN} = Re\left[f_{pN}(0)\right]/Im\left[f_{pN}(0)\right]$ the ratio of real-to-imaginary part of the forward pN scattering amplitude and β_{pN} is known as the slope parameter. The energy dependence of the parameters is taken into account by interpolating experimental values obtained from phase-shift analysis. This procedure is a source of additional systematical uncertainties which are taken into account in the final radii. The optical limit approximation was not used since it is known that it is not very accurate for spatially extended nuclei [13]. The nucleon density must be parametrized by choosing a suitable functional form. It is then very likely that the obtained result will be model-dependent, therefore one uses several mathematical forms and the final result is averaged over all individual values. Model parametrizations used in this analysis correspond to those used in Ref. [5]. They are all described by two parameters and can be resumed in two different classes:

1. in the first class, all nucleons have the same density form. These are the Woods-Saxon (**WS**), the Symmetrized Fermi (**SF**) and the Gaussian-Halo (**GH**) parametrizations

2. in the second class, a separate description is made for the core and halo nucleons. A gaussian form is chosen for the core nucleons while a gaussian (Gaussian-Gaussian **GG**) or a 1p-shell harmonic oscillator form (Gaussian-Harmonic Oscillator **GO**) is chosen for the halo nucleons. This class allows for the direct determination of the core and halo radii $R_{c,h}$. It should be noted, that for these parametrizations, an assumption is to be made for the number of halo nucleons.

In a χ^2 minimization procedure, the two descriptive parameters of each distribution are varied independently from each other and the resulting calculated cross section is compared to the experimental data in order to get the best possible fit. The detailed comparative analysis can be found in Ref. [14]. Being limited in space, only an informative example from the analysis of the ^6He case is shown here for the GG parametrization (Fig. 6). Two fits are shown where only data at low t (solid) and then combined data sets (dashed) - low and high t data - were taken into account. Keeping in mind that data at $t \simeq 0$ are necessary for the size determination, one can directly compare the individual value obtained by considering only the low t data, R_m=2.30 (5) fm with the new value obtained by including the present data, R_m=2.36 (2) fm. The size increased within the experimental uncertainties while the statistical uncertainty was reduced by a factor 2.

Individual nuclear matter densities and radii

The tables 1 and 2 resume the different matter radii values obtained for ^6He and ^8He respectively. The obtained χ^2_r and the resulting cross section (Fig. 6) prove that each parametrization is able to model the matter density distribution. All details can be found in Ref. [14]. The errors shown do not contain the systematical uncertainty contribution coming from the

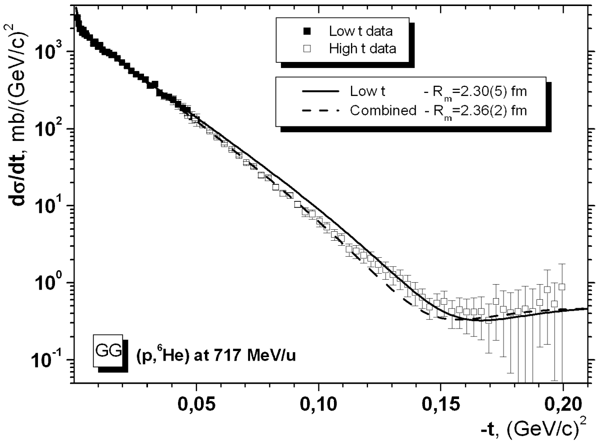

Figure 6: Calculated differential cross sections versus the four-momentum transfer squared $-t$ for the GG parametrization of ^6He for the data sets obtained at low t (full curve) and the combined data set (dashed curve) in comparison with the experimental data from Ref. [4] and from the present work.

		R_m (fm)	R_c (fm)	R_h (fm)	χ_r^2
WS	C	2.39 (2)			0.82
	L	2.30 (4)			0.75
SF	C	2.39 (2)			0.83
	L	2.31 (6)			0.75
GH	C	2.34 (2)			0.80
	L	2.29 (5)			0.76
GG	C	2.36 (2)	2.02 (1)	2.93 (6)	0.78
	L	2.30 (6)	1.95 (10)	2.88 (27)	0.77
GO	C	2.33 (2)	1.91 (1)	2.99 (4)	0.63
	L	2.30 (5)	1.81 (8)	3.03 (21)	0.76

Table 1: Summary of the total, core and halo radii (R_m, R_c, R_h) values after fitting the experimental (p,^{6} He) elastic differential cross section at 717 MeV/u. For every model parametrization, the fit results from the combined data set (C) and from the low t data [3, 5] (L) are presented. The reduced chi-square χ_r^2 is also reported. Uncertainties shown are individual statistical errors without systematical errors.

Glauber calculation and variations within the various model parametrizations. If one takes only these errors into account, a better precision is obtained on the matter radius R_m when including the present data in the analysis. The gain in accuracy is much more important in the case of the core radius R_c though a clear systematical discrepancy between the two models GG and GO, 0.11 fm for ^6He and 0.18 fm for ^8He to be compared with the obtained individual uncertainties of 0.01 fm. The deviation is less important in case of low t data analysis: the two values differ by 0.14 fm with a typical error of 0.10 fm. It will also degrade the precision on the final average R_c value.

Considering the total size R_m, a reasonable consistency is obtained for all the cases. The inclusion of the new data tend to systematically increase the size of ^6He while the size decreases in the ^8He case. The obtained individual matter densities can also be compared for ^6He as shown in Fig. 7. First, one notes the gain in precision in the central region, below 2 fm with the help of the data at high t. The five parametrizations give a similar description of the nuclear matter in the region below 5 fm.

		R_m (fm)	R_c (fm)	R_h (fm)	χ_r^2
WS	C	2.41 (2)			1.21
	L	2.48 (5)			1.10
SF	C	2.41 (2)			1.21
	L	2.46 (3)			1.10
GH	C	2.40 (3)			1.22
	L	2.47 (4)			1.09
GG	C	2.37 (4)	1.88 (1)	2.78 (4)	1.24
	L	2.46 (4)	1.68 (7)	3.04 (9)	1.09
GO	C	2.32 (2)	1.70 (1)	2.80 (3)	1.38
	L	2.42 (3)	1.42 (7)	3.12 (7)	1.10

Table 2: Summary of the total, core and halo radii (R_m, R_c, R_h) values after fitting the experimental (p,^{8} He) elastic differential cross section at 671 MeV/u. Same comments as Tab. 1

.

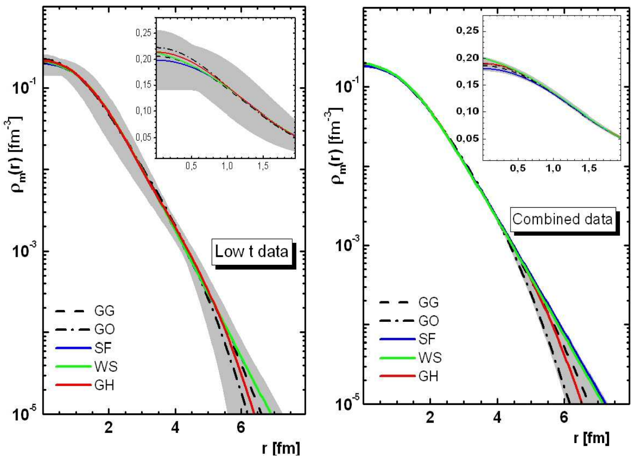

Figure 7: Total nuclear matter density distributions of ^6He deduced from the model parametrizations WS, SF, GH, GG and GO. Results are shown from fits with the low t data (left) and the combined data (right). The error corridor (shaded area) is the envelope including the uncertainties from all parametrizations without systematical uncertainties in the parameters of the pN amplitudes used in the Glauber calculation. Inserts give, in a linear scale, a more detailed view of the density distribution around the center of the nucleus.

Average nuclear matter densities and radii

The matter, core and halo radii obtained by different model parametrizations were averaged from the different models by using a weighted mean formula:

$$R = \frac{\sum R_i/\Delta R_i^2}{\sum 1/\Delta R_i^2} \tag{3}$$

The sum is made over the considered parametrizations i by using the corresponding radius R_i and its fit uncertainty ΔR_i. The final uncertainty ΔR is then the result of the following contributions:

- the fit error ΔR_{fit} which is the arithmetical mean of the ΔR_i
- the model uncertainty σ_R which measures the deviation of the individual values R_i to the mean value R by using the formulation $\sigma_R = \frac{\left[\sum (R_i - R)^2\right]^{1/2}}{N-1}$
- the systematical uncertainty from the Glauber model input parameters σ_{pN}, ε_{pN} and β_{pN} (Eq. 2) and an additional error arising from the uncertainty on the t-scale. The individual errors are 0.01, 0.02, 0.03 and 0.02 fm respectively.

Nucleus		R_m(fm)	R_c(fm)	R_h(fm)
^6He	C	2.36 (6)	1.97 (9)	2.97 (8)
	L [3]	2.30 (7)	1.88 (12)	2.97 (26)
^8He	C	2.38 (6)	1.79 (13)	2.79 (6)
	L [3]	2.45 (7)	1.55 (15)	3.09 (11)

Table 3: Matter, core and halo radii (R_m, R_c, R_h) obtained from the combined data set (C). Results [3] from the analysis in the low t range (L) are also shown for comparison.

The obtained averaged radii for both nuclei are shown in Tab. 3. The results at low t taken from Ref. [3], determined with the same procedure as described here, are also reported [2]. The total and core matter densities for each nucleus were also determined as an average. They are shown in Figs. 8 and 9 for ^6He and ^8He respectively. The corresponding uncertainty (shaded area), as

[2] It should be noted that in a more complete analysis [5] of the low t data, an additional contribution due to the tail of the nuclear matter distribution at the nucleus far periphery was taken into account on the basis of theoretical considerations [15]. This led to increase the R_m values shown in Tab. 3 by 0.15 fm and 0.08 fm for ^6He and ^8He, respectively.

in Fig. 7 for ^6He is obtained by including the errors from all models. In the case of ^6He, the description of the total matter is fairly similar when excluding or including the present data except in the peripheral region: the new estimate is larger than the previous one therefore the total matter radius increases. In the ^8He case, the matter density at the center decreases by a factor 2 while it remains the same in the higher r range: as a result the total size decreases as already mentioned.

Size of the $^{6,8}He$ core

It is important to know how much the core in ^6He and ^8He is modified with respect to a free α particle. The core matter density taken as the average from the GG and GO models is displayed in Figs. 8 and 9 together with the matter density of the free ^4He nucleus for which R_m=1.49 fm.

The old determination of the core size in ^6He, R_c=1.88 (12) fm (Tab. 3) which is larger than the free α particle size already suggests that the core is moving into the nucleus around the center-of-mass of the borromean system α+n+n. One measures in fact an apparent size which is a folding of the α particle size with the average CM motion amplitude. The new determination R_c=1.97 (9) fm strongly supports this finding.

In the case of ^8He, neither the old value, R_c=1.55 (15) fm (Tab. 3) nor the core matter density (bottom part of Fig. 9) which is overlapping the matter density of the free α particle could confirm this statement. With the new value, R_c=1.79 (13) fm and with the corresponding density (top part of Fig. 9) which is less dense in the center and more dense in the periphery than is the α particle matter density, it is clear that the core in ^8He also moves around the CM of the system but with a smaller amplitude. The effect of the relative motion on the core size by increasing the number of the valence neutrons was already predicted [16]. It can be directly observed here by comparing the ^6He and ^8He nuclei: adding more valence neutrons to the α core prevent it to extend more spatially which can be seen in the newly determined values $R_{c,^8He} \leq R_{c,^6He}$.

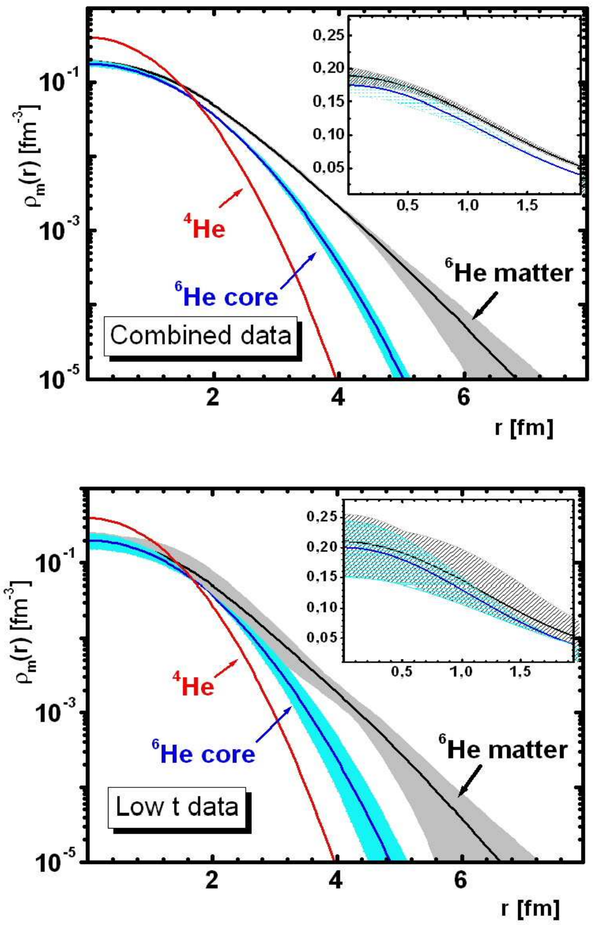

Figure 8: The average total (black) and core (blue) matter density distributions of ^6He as results from fits with the low t data (bottom) and the combined data (top). The error corridor (shaded area) is the envelope including the uncertainties from all the cited parametrizations and is identical to the one shown in Fig. 7 for the case of the total nuclear matter. Inserts give, in a linear scale, a more detailed view of the density distribution around the center of the nucleus. These distributions are compared to the case of free ^4He shown in red.

4 Conclusion

The previous study of $^{6,8}He$ nuclear matter density distributions using intermediate energy proton elastic scattering at low transfered momentum $0.002 \leq |t| \leq 0.05 (GeV/c)^2$ was sensitive to the outer structure of these nuclei. In the work presented here, a deeper

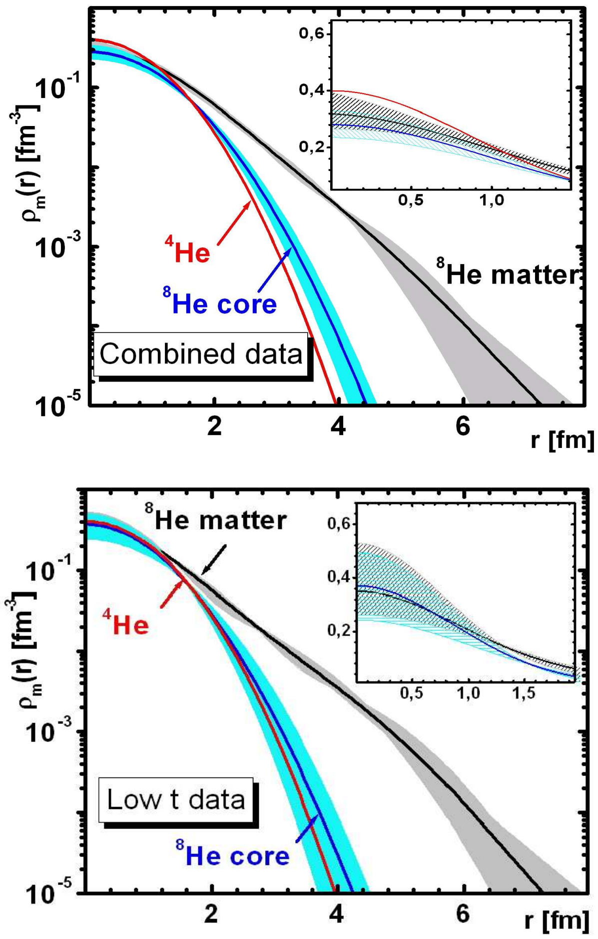

Figure 9: The average total (black) and core (blue) matter density distributions of ^8He as results from fits with the low t data (bottom) and the combined data (top). Same comments as in Fig. 8.

study of the inner part of these two nuclei was conducted in order to get a better perception on their structure. For this purpose, measurements were extended to the higher transfered momentum region $0.05 \leq |t| \leq 0.22(GeV/c)^2$, typically to the first diffraction minimum by using the same kinematical conditions. For the first time, a liquid-hydrogen target was successfully used in a reaction experiment with radioactive beams allowing measurements with a low background level. The new differential elastic cross sections obtained in this work agree well with the ones measured in the low t domain as seen from the region where both data overlap.

Cross sections were calculated within the framework of Glauber multiple scattering theory and fitted to the data in order to get the best possible description. Different parametrizations to model the nuclear matter density distributions were used. The available experimental data at low and high t were analysed separately and together, in order to determine the influence of the measurement domain on the final density distribution. The individual matter rms radii determined with the present data are, in general, consistent with the ones determined from the data at low transfered momentum. For a given data set, the different parametrizations are compatible within errors if systematical uncertainties from the Glauber calculation are included, which proves that the procedure used here is practically model independent.

The present data enable one to get a new set of density distributions with a high precision level which might certainly be used as input for other experimental and theoretical studies (inelastic scattering, transition amplitudes, etc ...). The new determined matter radii are 2.36(6) fm for ^6He and 2.38(6) fm for ^8He. In the present research state, these values are still to be considered preliminary and it is certainly too early to draw any definite conclusion from that. In particular for the considered t range, a more refined analysis must be used including (i) a proper treatment of the center-of-mass correlations and (ii) a more complete parametrization of the NN interaction amplitude taking into account the spin dependent part.

The effective core size R_c of both nuclei is bigger than the free ^4He size: this feature was already reported in the case of ^6He and is confirmed by the new measurement. In the case of ^8He, this observation is possible only if the present data are taken into account. It is interpreted as the result of the relative motion of an α core with an intrinsic size close to 1.49 fm around the core-halo center-of-mass.

Acknowledgements

This work was supported by the German Federal Ministry for Education and Research and Russian Ministry for Technology and Science under the contract WTZ RUS 621/96.

References

[1] K. Riisager, Rev. Mod. Phys. 66 (1994) 1105

[2] P. G. Hansen, A. S. Jensen and B. Jonsson, Ann. Rev. Nucl. Part. Sci. 45 (1995) 591

[3] G.D. Alkhazov *et al.*, Phys. Rev. Lett. 78 (1997) 2313

[4] S.R. Neumaier *et al.*, Nucl. Phys. A712 (2002) 247

[5] G.D. Alkhazov *et al.*, Nucl. Phys. A712 (2002) 269

[6] L.V. Chulkov et al., Nucl. Phys. A587 (1995) 291

[7] M. V. Zhukov *et al.*, Phys. Rev. C50 (1994) R1-R4

[8] H. Geissel *et al.*, Nucl. Instr. and Meth. B70 (1992) 286

[9] G.D. Alkhazov *et al.*, Phys. Rep. 42 (1978) 89

[10] A. G. Sitenko, Theory Of Nuclear Reactions, World Scientific, 1990

[11] R. J. Glauber, Lectures in theoretical physics - High-energy collision theory, W. E. Brittin, Interscience, New York, Vol.I (1959) 315

[12] R. J. Glauber, Proceedings of the 3rd International Conference on High Energy Physics and Nuclear Structure, Theory of High Energy Hadron-Nucleus Collisions, New York, USA, 1970

[13] Y. Ogawa *et al.*, Phys. Lett. B543 (1992) 722

[14] F. Aksouh, PhD Thesis, Université de Paris XI, Orsay, France, 2002

[15] J. S. Al-Khalili, J. A. Tostevin, Phys. Rev. C57 (1998) 1846

[16] G. P. Kamuntaviõius, Phys. Rev. C56 (1997) 191